A finite element investigation of quasi-static and dynamic asymptotic crack-tip fields in hardening elastic–plastic solids under plane stress

Part I: Crack growth in linear hardening materials

XIAOMIN DENG* and ARES J. ROSAKIS
*California Institute of Technology, Pasadena, California 91125, USA; *present address: Department of Mechanical Engineering, University of South Carolina, Columbia, South Carolina 29208, USA*

Abstract. The asymptotic structures of crack-tip stress and deformation fields are investigated numerically for quasi-static and dynamic crack growth in isotropic linear hardening elastic–plastic solids under mode I, plane stress, and small-scale yielding conditions. An Eulerian type finite element scheme is employed. The materials are assumed to obey the von Mises yield criterion and the associated flow rule. The ratio of the crack-tip plastic zone size to that of the element nearest to the crack tip is of the order of 1.6×10^4. The results of this study strongly suggest the existence of crack-tip stress and strain singularities of the type r^s ($s < 0$) at $r = 0$, where r is the distance to the crack tip, which confirms the asymptotic solutions of variable-separable type by Amazigo and Hutchinson [1] and Ponte Castañeda [2] for quasi-static crack growth, and by Achenbach, Kanninen and Popelar [3] for dynamic crack propagation. Both the values of the parameter s and the angular stress and velocity field variations from the present full-field finite element analysis agree very well with those from the analytical solutions. It is found that the dominance zone of the r^s-singularity is quite large compared to the size of the crack-tip active plastic zone. The effects of hardening and inertia on the crack-tip fields as well as on the shape and size of the crack-tip active plastic zone are also studied in detail. It is discovered that as the level of hardening decreases and the crack propagation speed increases, a secondary yield zone emerges along the crack flank, and kinks in stress and velocity angular variations begin to develop. This dynamic phenomenon observable only for rapid crack growth and for low hardening materials may explain the numerical difficulties, in obtaining solutions for such cases, encountered by Achenbach et al. who, in their asymptotic analysis, neglected the existence of reverse yielding zones along the crack surfaces.

1. Introduction

For quasi-static crack growth in isotropic, linear hardening elastic-plastic solids, Amazigo and Hutchinson [1] performed asymptotic analyses in mode III and in mode I plane stress and plane strain through variable-separable solutions. By assuming the existence of an active plastic zone at the crack front, and by neglecting the possible reverse plastic loading along the traction-free crack surface, they were able to obtain angular variations of the crack-tip stress and plastic strain rate fields, and to determine their order of singularities at the crack tip.

The above analyses were generalized in mode III by Dunayevsky and Achenbach [4] for low hardening materials so as to approach the elastic-perfectly plastic solution when hardening disappears, and were extended in mode III and mode I plane stress and plane strain to include a secondary plastic zone along the crack flank by Ponte Castañeda [2], who also introduced a novel method for obtaining an approximate amplitude factor of the near-tip singular field and approximate crack-tip active plastic zone shapes.

Finite element studies under steady state and small-scale yielding conditions were carried out by Dean and Hutchinson [6] in mode III, with comparisons to the asymptotic results of Amazigo and Hutchinson [1], and by Dean [7] in mode I plane stress. Both of the studies gave

explicit results regarding the crack-tip opening displacement variations and the effect of hardening on the shape of the crack-tip primary active plastic zone.

For an isotropic hardening material, the effect of yield-surface vertices was considered by Lo and Peirce [8] in mode III, with a phenomenological J_2 corner theory of plasticity [9]. An analysis for mode I plane strain, steady state, quasi-static crack growth was performed by Zhang, Zhang, and Hwang [10] to study Bauschinger-like effects for anisotropic linear hardening solids. Finite element computations for steady state, quasi-static crack growth conducted by Lam [11] and Lam and McMeeking [12] in mode I plane strain also investigated the effect of kinematic hardening with a bilinear stress strain relation.

Under dynamic crack propagation conditions, the asymptotic quasi-static solutions of variable-separable type by Amazigo and Hutchinson [1] were extended for isotropic linear hardening materials to include inertia by Achenbach and Kanninen [13] in mode III, and Achenbach, Kanninen, and Popelar [3] in mode I plane stress and plane strain. It is noted that both of the above studies neglected the possible reverse plastic loading along the crack flank, which may yield large errors when this secondary plastic zone is large.

In the following, we will report the results of a very detailed finite element investigation of the crack-tip fields for cracks growing, quasi-statically or dynamically, in isotropic, linear hardening solids, under conditions of mode I plane stress, steady state, and small-scale yielding. We will compare the solutions of this study to available asymptotic and numerical counterparts in the literature. Detailed discussions regarding the evolutionary variations of the field quantities with respect to crack propagation speed and the effect of linear strain hardening on the crack-tip fields will be presented. All computations are carried out with Poisson's ratio $v = 0.3$. All logarithmic values used in figures are based on the natural number e.

The finite element formulation employed in this study is of the Eulerian type, which was first used in fracture mechanics by Dean and Hutchinson [6]. Stresses are obtained by numerically integrating the incremental elastic–plastic constitutive law over strain increments, with the *modified tangent predictor-radial return algorithm* [14]. This stress integration algorithm conbines the fine points of both the original *tangent predictor-radial return algorithm* [15] and the *secant stiffness algorithm* [16, 17], in that it is easy to implement in plane stress, and that it gives a stress state automatically satisfying the yield condition at the end of a strain increment for elastic-perfectly plastic and linear hardening materials.

In implementing the stress integration algorithm, a solution procedure proposed by Deng and Rosakis [18] is adopted. With this technique, existing solution procedures in wide use today can be modified to eliminate the occurrence of negative plastic flow, and to avoid treating elastic unloading as plastic flow. This modification is shown to improve the accuracy and convergence of the numerical solution.

2. Finite element formulation

In this section, the finite element formulation and the design of the finite element mesh are discussed briefly. Details can be found in [14, 18].

The linear hardening material under consideration is assumed to be homogeneous, isotropic, and obey the von Mises yield condition and the associated flow rule. As we know, the uniaxial stress-strain curve for such a material is depicted by two straight lines: the elastic line and the plastic line, with slopes E and E_p respectively. The ratio of the two slopes, $\alpha = E_p/E$, is called

the hardening parameter and represents the hardening level of the material. Obviously, when $\alpha = 1$, the material is linearly elastic; when $\alpha = 0$, the material is elastic-perfectly plastic.

Suppose a crack is propagating steadily in a plane made of such a material (see Fig. 2.1), such that an observer moving with the crack tip will not see any changes of the crack-tip fields as the crack extends. Mathematically, this requires that the crack speed v be a constant, and that for any field quantity, say, q, its material time derivative be computed from

$$\frac{\partial q}{\partial t} = -v \frac{\partial q}{\partial x_1}. \tag{2.1}$$

Equation (2.1) implies that the time rate or history of any field quantity for steady-state crack growth is stored spatially along horizontal lines parallel to the direction of crack propagation.

Making use of the property specified by (2.1), an iterative finite element solution procedure first used by Dean and Hutchinson [6] is adopted in this study. In the present study, at each solution step, convergence is said to have been reached at the $(k + 1)$th iteration if the following criterion is met simultaneously for every choice of i, j and α

$$\frac{\|\sigma_{ij}^{k+1} - \sigma_{ij}^{k}\|_2}{\|\sigma_{ij}^{k+1}\|_2} \leqslant \varepsilon, \quad \frac{\|\varepsilon_{ij}^{k+1} - \varepsilon_{ij}^{k}\|_2}{\|\varepsilon_{ij}^{k+1}\|_2} \leqslant \varepsilon, \quad \frac{\|u_{\alpha}^{k+1} - u_{\alpha}^{k}\|_2}{\|u_{\alpha}^{k+1}\|_2} \leqslant \varepsilon, \tag{2.2}$$

where σ_{ij}, ε_{ij} and u_{α} represent respectively the stress, strain, and displacement components; indices i, j range from 1 to 3 and α from 1 to 2; $\|\cdot\|_2$ is the standard 2-norm; and ε is the error tolerance which is a small positive number. The stress and strain norms are summed over all Gauss integration points, and the displacement norm is summed over all nodal points. ε is taken to be around 1.0×10^{-4} in the current computation.

In this study, the small-scale yielding condition [19, 20] is assumed. A rectangular domain of finite size (see Fig. 2.2) is used to model the mathematical problem of a semi-infinite crack advancing in an otherwise infinite plate, where coordinates x_1 and x_2 are normalized by $(K/\sigma_0)^2$, K being a generic symbol for the stress intensity factor, and σ_0 the initial yield stress in
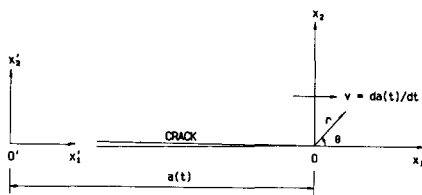
Fig. 2.1. A diagram of crack propagation, where (x_1', x_2') is a fixed reference coordinate system; (x_1, x_2) is a moving system with origin at the crack tip; and (r, θ) is the associated polar coordinate system.
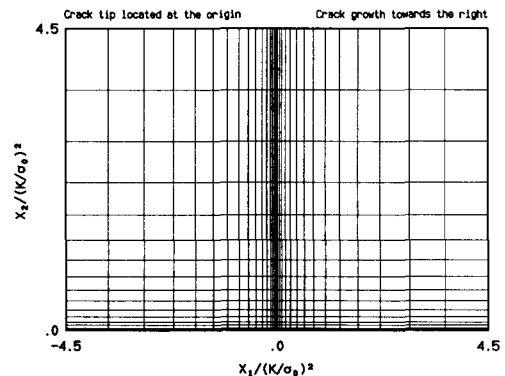
Fig. 2.2. A coarse representation of the finite element mesh used in the present computation.

uniaxial tension. The origin of the schematic mesh in Fig. 2.2 is at the current crack tip, and the traction-free crack surface and the symmetry line coincide, respectively, with the negative and positive x_1-axis. The domain of the rectangle is discretized by a network of horizontal and vertical lines, whose intervals decrease rapidly towards the bottom and the center vertical lines, resulting in vanishingly small elements near the crack tip. The divided areas are simply represented by four-noded isoparametric rectangular elements, with 2×2 Gauss integration points. This type of element arrangement is designed to fit the need of the Eulerian finite element formulation, such that stresses can be integrated along horizontal lines composed of Gauss points, from the right boundary to the left (for details, see [14]). Now according to the boundary layer concept introduced by Rice [19, 20], the solution for this mathematical problem is equivalent to the crack-tip solution for the original mechanics problem under small-scale yielding conditions. As pointed out by Dean [7], a domain with a size larger than ten times that of the crack-tip active plastic zone will suffice to produce reasonable results. The size employed in this investigation is about fifteen times larger than the plastic zone size.

Two meshes of high resolution are used in our computation. They are different in that the numbers of the horizontal and vertical lines of the mesh networks and the variations of the intervals between those lines are different. In the finer mesh, the network of lines results in 4050 elements with 4186 nodes, and the ratio of the plastic zone size to that of the smallest near-tip element is on the order of 1.6×10^4. In the sightly coarser mesh, there are 1800 elements, and the plastic zone size is about 0.8×10^4 times the size of the smallest near-tip element. Comparisons between numerical results obtained from those two meshes demonstrate very good agreement, which was reported earlier in [14, 23].

The boundary condition is specified as follows. In accordance with the small-scale yielding assumption, surface traction and displacements corresponding to the crack-tip elastic singular field, which is characterized uniquely by the dynamic stress intensity factor K_1^d, are prescribed on the domain boundary, with necessary updating on the portion of the boundary near the crack flank, where boundary conditions incompatible with the K-field arise due to the presence of residual plasticity in the plastic wake.

3. Quasi-static crack growth

As mentioned in the introductory section, quasi-static crack growth in linear hardening solids under mode I plane stress and steady state conditions has been investigated through asymptotic analyses of variable-separable type by Amazigo and Hutchinson [1] and by Ponte Castañeda [2], and through a finite element analysis of the Eulerian type under small-scale yielding conditions by Dean [7]. Explicit results were obtained by Amazigo and Hutchinson and Ponte Castañeda regarding the singularities and angular variations of the crack-tip asymptotic stress and velocity fields, and by Dean regarding the shape of the crack-tip active plastic zone and the radial dependence of the crack opening profile. In the following subsections, comparisons of the present numerical solution with those mentioned above will be performed whenever possible.

3.1. Active plastic zones

Approximations for the shapes of the crack-tip active plastic zones under small-scale yield-ing conditions have been given by Dean [7], from a finite element analysis very similar to

the present one, and by Ponte Castañeda [5], through matching trial functions to the elastic far-field and the elastic–plastic near-tip field, with parameters optimized using a variational compatibility statement. Comparisons with the results of the previous two investigations are shown in Fig. 3.1 for $\alpha = 0.25$ and 0.1, where α is the hardening parameter. Note that the Poisson's ratio is taken to be 0.5 in Ponte Castañeda's calculation, and 0.3 in those of Dean and the current authors. It is seen from Fig. 3.1a, as in the case of ideal plasticity (see Fig. 3.2.1 of [14]), Dean's result predicts a plastic zone larger than ours. Considering the fact that the current study employed a much finer near-tip finite element mesh, it is felt that the current study gives a better approximation for the crack-tip active plastic zone.

As to the comparisons with Ponte Castañeda's result, it is seen from Fig. 3.1b that both calculations agree well on the size of the active plastic zone along the prospective crack line, and on the angular extent of the active plastic zone. Yet Ponte Castañeda's approximation estimated a much higher value for the height of the active plastic zone than ours. It should be noted that Ponte Castañeda's result also gave a large plastic zone size in mode III, but in the horizontal direction rather than in the vertical direction. Nonetheless, due to the use of different Poisson's ratio values, it is difficult to draw definite conclusions from the above comparison.

The effect of hardening on the shape of the crack-tip active plastic zone is illustrated in Fig. 3.2. It is found that as the level of strain hardening decreases (i.e. as α decreases), the size of the active plastic zone increases from $0.168(K/\sigma_0)^2$ at $\alpha = 0.5$ to $0.209(K/\sigma_0)^2$ at $\alpha = 0.1$ in the horizontal direction, and it decreases from $0.179(K/\sigma_0)^2$ at $\alpha = 0.5$ to $0.140(K/\sigma_0)^2$ at $\alpha = 0.1$ in the vertical direction.

Estimate for the angular extent of the active plastic zone or the angle at which elastic unloading occurs is very sensitive to the contour value used in the estimation. Consequently, this subject will be temporarily dropped until the angular variation of the stress field is discussed. Moreover, it is worth mentioning that there are no signs of the existence of secondary active plastic zones at the back of the quasi-statically growing crack tip for the hardening parameter values studied. This observation will be further discussed later.
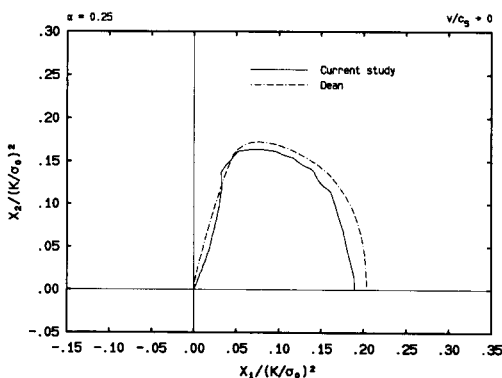
Fig. 3.1a. A comparison of the crack-tip active plastic zone in normalized coordinates with that of Dean [7] for $\alpha = 0.25$, with the crack tip situated at the origin.
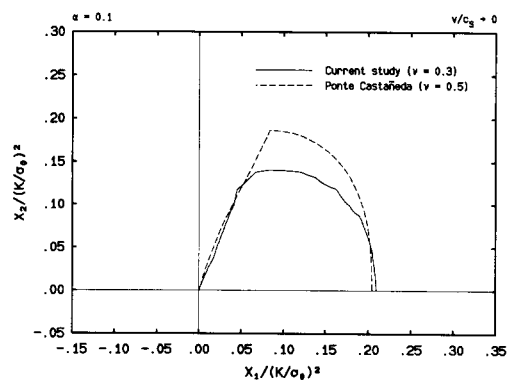
Fig. 3.1b. A comparison of the crack-tip active plastic zone in normalized coordinates with that of Ponte Castañeda [5] for $\alpha = 0.1$, with the crack tip situated at the origin.

3.2. Angular field variations

We present the crack-tip stress and velocity field variations in this subsection. We start with a comparison of stress variations with the asymptotic solutions of Ponte Castañeda [2] for $\alpha = 0.1$. (Although this asymptotic solution was carried out with Poisson's ratio $v = 0.5$, it is still comparable with the present study due to the existence of substantial incompressible plastic deformation at the crack tip). Angular variations of polar stress components σ_{rr}, $\sigma_{\theta\theta}$ and $\sigma_{r\theta}$, von Mises's effective stress σ_e, and flow stress or the current yield stress σ for the current yield surface, are plotted in Fig. 3.3, which demonstrate very good agreement between the analytical results ($v = 0.5$) and the finite element results ($v = 0.3$). We also note that the asymptotic analysis in [2] predicts that elastic unloading occurs at an angle around $73.65°$, which is right at the angular position where the effective stress becomes smaller than the flow stress (see Fig. 3.3). On one hand, this comparison suggests that the Poisson's ratio has little effect on the stress variation near the crack tip, which can be attributed to the fact that when $\alpha = 0.1$ the elastic part of the strains is small compared to its plastic counterpart. On the other hand, this good agreement indicates that the present finite element mesh is fine enough to capture the asymptotic behavior of the crack-tip stress and deformation fields. Consequently, the findings of this numerical study can be interpreted with greater confidence.

The effect of hardening on the angular stress variations are demonstrated through the progressive changes of stress components with respect to the linear hardening parameter α, as shown in Fig. 3.4, where all stress quantities are normalized such that $\sigma_e = 1$ at $\theta = 0$. The general tendencies of the stress variations are consistent with the asymptotic solutions in [1], which were later elaborated in [2] as discussed earlier. Further, the numerical solution seems to show that the slopes of σ_{rr} at $\theta = 0$ and $\sigma_{\theta\theta}$ at $\theta = 0$ and $180°$, are very close to zero for all α values computed. Substantial compressive radial stresses behind the crack tip are observed also for all α values studied, which suggests, as in the case of ideal plasticity (see [23]), that a tendency of reverse loading exists at the back of the crack tip. However, it is clear, as indicated by the relative magnitudes of the effective stress σ_e and the flow stress σ, that this tendency is not strong enough for the stress state near the crack surface to regain yielding. This is consistent
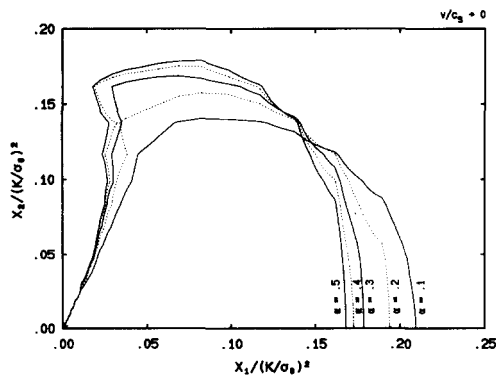
Fig. 3.2. The effect of hardening on the crack-tip active plastic zone in normalized coordinates, with the crack tip situated at the origin.
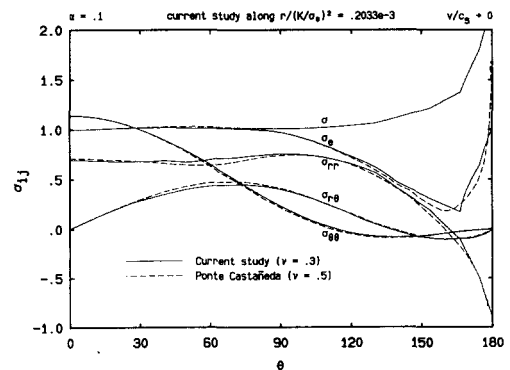
Fig. 3.3. Angular variations of the polar stress components, the effective stress σ_e, and the flow stress σ for $\alpha = 0.1$, normalized such that $\sigma_e = 1$ at $\theta = 0$, with comparison to the asymptotic solution by Ponte Castañeda [2].
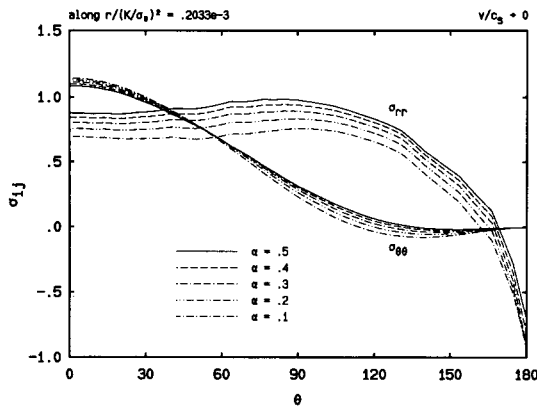
Fig. 3.4a. The effect of hardening on the angular variations of the polar stress components σ_{rr} and $\sigma_{\theta\theta}$, normalized such that the effective stress $\sigma_e = 1$ at $\theta = 0$.
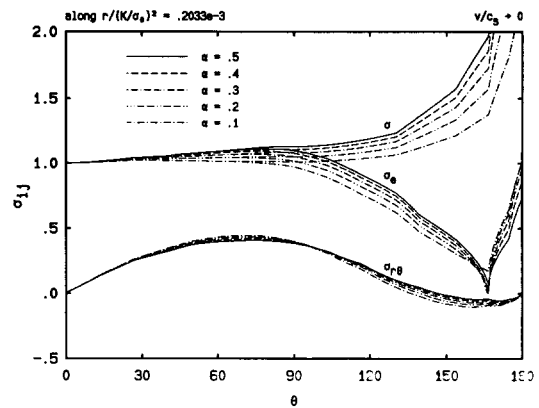
Fig. 3.4b. The effect of hardening on the angular variations of the polar stress component $\sigma_{r\theta}$, the effective stress σ_e, and the flow stress σ, normalized such that $\sigma_e = 1$ at $\theta = 0$.

with existing analytical solutions. For example, according to the asymptotic solution in [2], plastic reloading occurs only for $\alpha \leqslant 0.01$ and at an angle very close to 180°. Hence, the plane stress solution in [1], which neglected the possibility of plastic reloading behind the crack tip, is indeed a very accurate simplification. It can be further observed from Fig. 3.4 that the value of $\sigma_{\theta\theta}$ is very close to zero near the crack flank from $\theta = 165°$ to 180°, and that the traction-free condition at $\theta = 180°$ is very well satisfied, which is a major sign of the convergence of numerical solutions obtained from an Eulerian type finite element procedure.

The angular extent of the crack-tip active plastic zone or the angle at which elastic unloading occurs can be estimated from the position where σ_e deviates from σ, with an error tolerance specified for the relative difference of the two quantities. For example, we can set the tolerance to be the value such that for $\alpha = 0.1$, the numerically estimated angle equals that of the analytic study in [2], which is approximately 0.77×10^{-2}. Then the angle for the active plastic zone is estimated to be, for example, 77.9° for $\alpha = 0.5$ and 72.4° for $\alpha = 0.05$. We have compared these estimates for different α values with those of [2] with satisfactory agreement.

The angular variations of the Cartesian velocity components for $\alpha = 0.1$, with good agreement with those of [2], are shown in Fig. 3.5, where the velocity quantities are normalized such that $v_1 = -1$ at $\theta = 0$. The dependence on α of the angular velocity variations is illustrated in Fig. 3.6, with the same normalization. It can be seen that v_1 and v_2, respectively, always stay negative and positive. At $\theta = 0$, the slope of v_2 is found to increase as α decreases. At angles beyond the active plastic zone, approximately for θ larger than 70°, the magnitude of v_2 is about three times that of v_1.

3.3. Radial field variations

The radial variations of the crack-tip stress and strain fields will be presented along the prospective crack line ($\theta = 0$) and for stress component σ_{22} and plastic strain component ε_{22}^p only. Their features, however, are typical of the variations of other stress and strain components and along other radial lines (see [14]). All data are taken from five elements away from the crack tip and only one data point is extracted from each element. While plotted radial variations in original coordinates can be found in [14], those shown here are often illustrated in nondimensional double-logarithmic (natural logarithm) coordinates only.
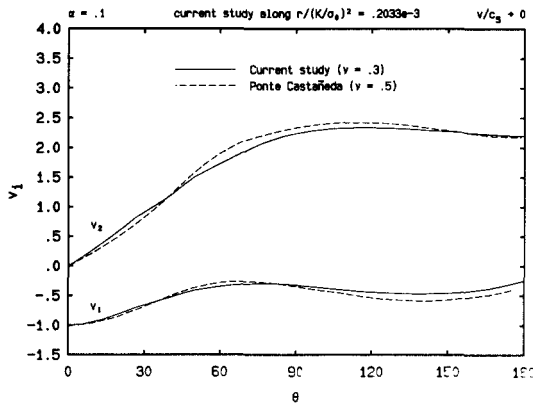
Fig. 3.5. Angular variations of the Cartesian velocity components for $\alpha = 0.1$, normalized such that $v_1 = -1$ at $\theta = 0$, with comparison to the asymptotic solution by Ponte Castañeda [2].
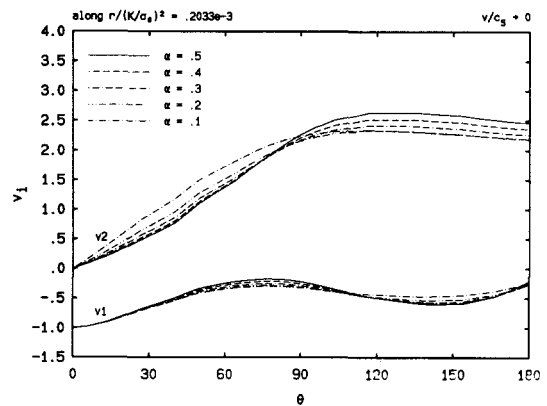
Fig. 3.6. The effect of hardening on the angular variations of the Cartesian velocity components, normalized such that $v_1 = -1$ at $\theta = 0$.

The general trend of the stress variations are as follows. It is observed that all stress components possess strong singularity at the crack tip, and that the magnitudes of their radial distribution decrease as α, the level of strain hardening, decreases. As shown in Fig. 3.7 in double-logarithmic coordinates, where the data point on the left is nearest the crack tip, the stress distributions for σ_{22} for materials with different levels of strain hardening, all appear as straight lines within a sizable crack-tip region (see Table 3.2). It can be concluded then that the stresses must behave asymptotically at the crack tip as r^s ($s < 0$) as $r \to 0$, where the singularity parameter s equals the slope of the straight lines. Since the absolute value of s and the magnitudes of the stress components are found to decrease as α decreases, it can be said that the stresses are less singular for materials with lower levels of strain hardening. Also from Fig. 3.7, it is seen that the straight lines start to curve up at locations away from the crack tip, especially so for smaller α values. In other words, the range of linearity of the curves becomes smaller as α becomes smaller. A consequence of this behaviour is that the dominance zone of the r^s-singularity diminishes as strain hardening disappears.

Similar observations can be made about strain variations. For example, the dependence of the plastic strain component ε_{22}^p on the radial distance r is plotted in double-logarithmic coordinates in Fig. 3.8, where the curves are seen to be nearly straight. Hence we conclude that plastic strains have the same type of singularities as stresses at the crack tip, behaving as r^s ($s < 0$) as the crack tip is approached, where $|s|$ decreases as α decreases.

As discussed earlier, Amazigo and Hutchinson [1] and later Ponte Castañeda [2] were able to obtain asymptotic solutions for stress and velocity fields with assumed r^s-type singularities. The angular stress and velocity variations and the values of s were obtained numerically from a system of ordinary differential equations in θ (derived from governing field equations with the assumed stress and velocity forms) subjected to appropriate boundary and continuity conditions. The magnitude of the field quantities and the size of the validity zone of the r^s-singularity are left undetermined in the asymptotic analyses and must be obtained from a complete boundary-value solution for a particular problem, such as from the present study.

To compare with the aforementioned analytic solutions regarding the values of s for materials with different values of α, least square fittings are performed for stress values found in the present finite element study. The stress data are taken along $\theta = 0$ from the sixth to the tenth
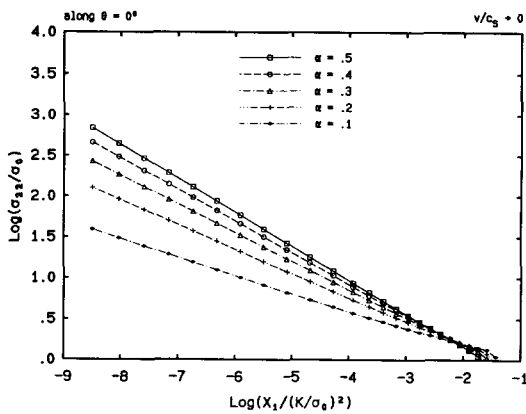
Fig. 3.7. Radial variations of the stress component σ_{22} along the prospective crack line in normalized double-logarithmic coordinates.
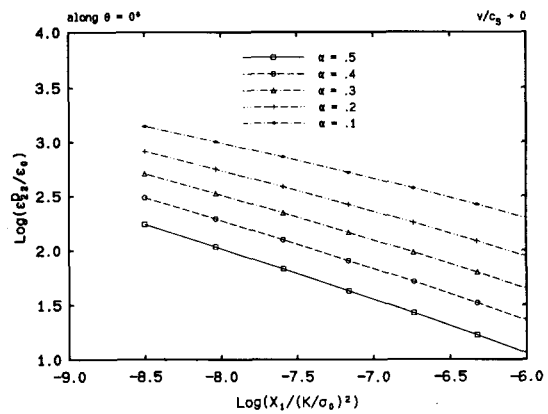
Fig. 3.8. Radial variations of the plastic strain component ε_{22}^p along the prospective crack line in normalized double-logarithmic coordinates.

elements (assuming the crack tip coincides with the lower-left node of the first element). Values of s are estimated for each stress component and their mean value is taken as the final estimate. The result of the estimations are listed in Table 3.1, where s_1 is the estimate from σ_{11}; s_2 is from σ_{22}; s_a is the average of s_1 and s_2; s_r is the reference value from the asymptotic solution in [2] for Poisson ratio $v = 0.5$; ε is the percentage relative difference of s_a from s_r. It is observed that the difference between the finite element results and the asymptotic results is consistently small. At the same time, it is observed that the difference increases as α decreases. This is expected since as the strain hardening becomes weaker, the dominance zone of the r^s-singularity becomes smaller, and hence the error becomes larger in approximating the stress curves as straight lines in the double-logarithmic coordinates.

The size of the r^s-singularity dominance zone can be estimated by setting a relative error tolerance between the original numerical data and the fitted data. For example, by requiring that the tolerance be within 5 percent, we have obtained such estimates along $\theta = 0$, which are shown in Table 3.2, where R_1 and R_2, normalized by the horizontal size of the crack-tip active plastic zone, are respectively the sizes of the dominance zones of stress components σ_{11} and σ_{22} with actual maximum relative percentage errors E_1 and E_2. The comparisons suggest that σ_{22} has

Table 3.1. Values of s for quasi-static crack growth

α	s_1	s_2	s_a	s_r	ε
0.5	−0.412	−0.416	−0.414	−0.420	−1.4
0.3	−0.346	−0.352	−0.349	−0.357	−2.2
0.2	−0.297	−0.303	−0.300	−0.310	−3.2
0.1	−0.223	−0.228	−0.225	−0.237	−5.1

Table 3.2. Dominance-zone size for r^s-type stress singularity for quasi-static crack growth

α	R_1	E_1	R_2	E_2
0.5	0.640	4.9	1.43	4.4
0.3	0.234	4.6	0.838	4.8
0.2	0.170	5.0	0.467	4.6
0.1	0.094	4.4	0.247	4.7
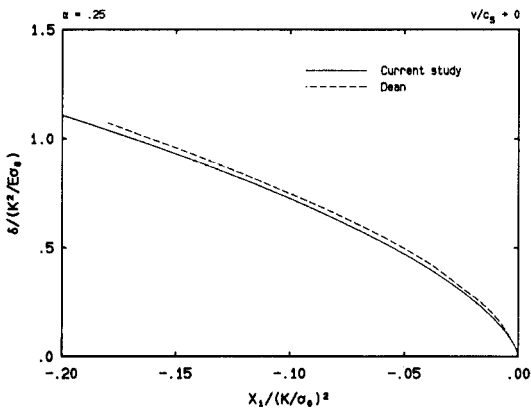
Fig. 3.9. The crack opening displacement δ (twice the vertical displacement u_2 along the crack surface) in normalized coordinates, compared to the finite element solution by Dean [7].
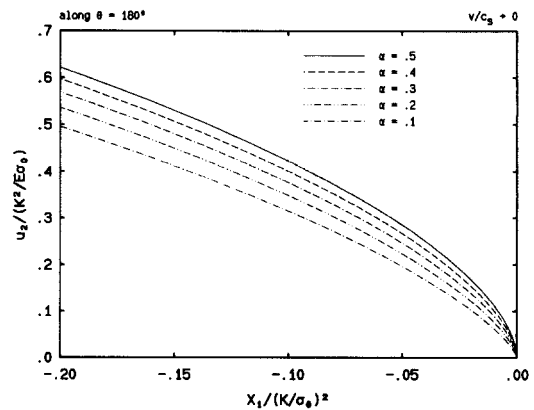
Fig. 3.10. The effect of hardening on the radial variation of the vertical displacement u_2 along the crack surface in normalized coordinates.

a much larger dominance zone than σ_{11} for all hardening values considered. Further, it is seen that the sizes of the dominance zones for both stress components decrease rapidly as α decreases. Nonetheless, it seems that the r^s-type stress singularity has a crack-tip dominance zone that is significant compared with the size of the active plastic zone even for materials with moderate strain hardening.

The radial dependence of displacement component u_2 along the crack surface is illustrated in Figs. 3.9 and 3.10. For $\alpha = 0.25$, the crack opening displacement δ, which is twice the value of u_2 along $\theta = 180°$, is compared with that of a similar finite element investigation by Dean [7]. As shown in Fig. 3.9, it is seen that δ predicted in [7] is slightly larger than that of the current study, which is believed to be due to the use of a coarser mesh employed in [7]. The dependence of the crack opening profile on the level of strain hardening is clearly shown in Fig. 3.10. It is obvious that u_2 decreases as α decreases.

4. Dynamic crack propagation

As outlined in the introduction, dynamic crack propagation in linear hardening solids under mode I plane stress and steady state conditions has been investigated by Achenbach, Kanninen, and Popelar [3] through asymptotic analyses of assumed variable-separable forms, in a manner similar to that by Amazigo and Hutchinson [1] for quasi-static crack growth. Explicit results were obtained of the crack-tip stress and velocity singularities, and the angular variations of stresses in the active plastic zone. In the following, these analytic results will be compared with those of the present finite element study whenever possible.

4.1. Active plastic zones

Shown in Fig. 4.1 is the effect of hardening on the shape of the crack-tip active plastic zone for $m = 0.3$, where m is the Mach number and is defined as the ratio of the crack propagation speed v to the material's elastic shear wave speed c_s. As in quasi-static crack growth, it is observed that as the level of strain hardening α decreases, the active plastic zone elongates in the direction of crack growth and shrinks in the perpendicular direction. Approximately, the width and height
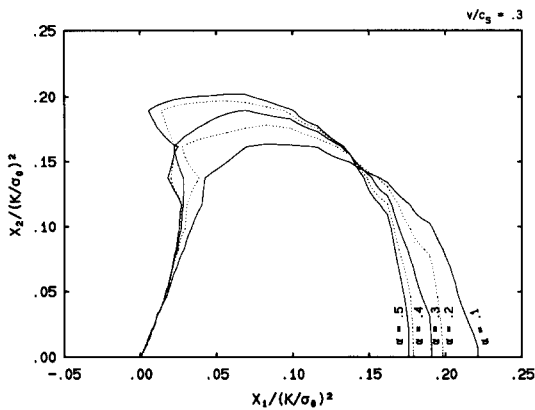
Fig. 4.1. The effect of hardening on the crack-tip active plastic zone for $v/c_s = 0.3$ in normalized coordinates, with the crack tip situated at the origin.
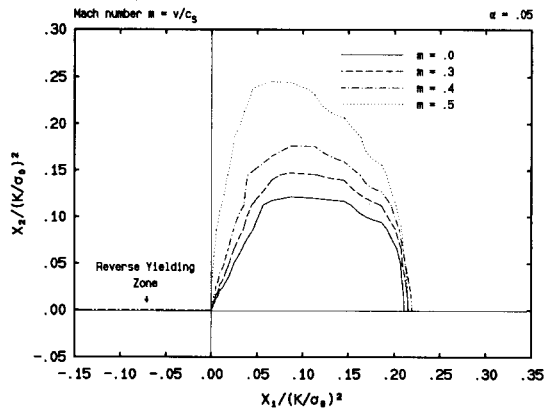
Fig. 4.2. The effect of crack propagation speed on the crack-tip active plastic zone for $\alpha = 0.05$ in normalized coordinates, with the crack tip situated at the origin.

of the plastic zone are, respectively, $0.177(K/\sigma_0)^2$ and $0.202(K/\sigma_0)^2$ when $\alpha = 0.5$, and $0.221(K/\sigma_0)^2$ and $0.164(K/\sigma_0)^2$ when $\alpha = 0.1$. Interestingly, the near-tip angular extent of the plastic zone, or the unloading angle, remains almost constant as α changes. When crack speed goes higher, however, the influence of the level of strain hardening bears different features. For example, when $m = 0.5$, the plastic zone does not change its size as significantly as when $m = 0.3$, but its shape varies in a different fashion when α varies. Furthermore, the near-tip angular extent of the plastic zone is found to increase as α decreases, and eventually a secondary active plastic zone develops along the crack surface as α approaches zero. This phenomenon is not observed when m is small.

The evolutionary variations of the crack-tip active plastic zone with respect to the crack propagation speed is illustrated in Fig. 4.2 for a material with weak strain hardening ($\alpha = 0.05$). The figure clearly shows that inertia has a strong effect on the height and angular extent of the plastic zone – as inertia or m increases, the height and the angular extent of the plastic zone increase substantially. However, for a material with a higher α value, the change in the angular extent is not as impressive. Again, a reverse yielding zone is observed along the crack flank when m becomes large. From the above findings, it can be concluded that the existence of a secondary active plastic zone along the crack surface is possible when crack speed is sufficiently high and for a material with a sufficient low level of strain hardening. It is noted, however, that the reversed plastic loading is limited to a region very close to the crack flank.

4.2. Angular field variations

In Fig. 4.3 the angular variations of the Cartesian stress components σ_{ij}, the effective stress σ_e and the current flow stress σ are plotted against the angular position θ for the case of $\alpha = 0.3$ and $m = 0.4$. The results of the asymptotic analysis in [3] for the same value of α and a slightly higher value of m (approximately equal to 0.403, corresponding to $\beta = 0.25$ of [3]), are plotted in the same figure. For comparison purposes, all stress quantities are normalized such that $\sigma_e = 1$ at $\theta = 0°$. It is clear that the two sets of angular stress variations agree very well. Note that the solutions from [3] stop at the angle at which elastic unloading takes place and which is found to be around 85.8°. As in the quasi-static case, this angle can be estimated from the numerical solution by locating the angular position where σ_e starts to deviate from σ. Using the error tolerance 0.77×10^{-2}, the angle is found to be about 81°, which is slightly smaller than
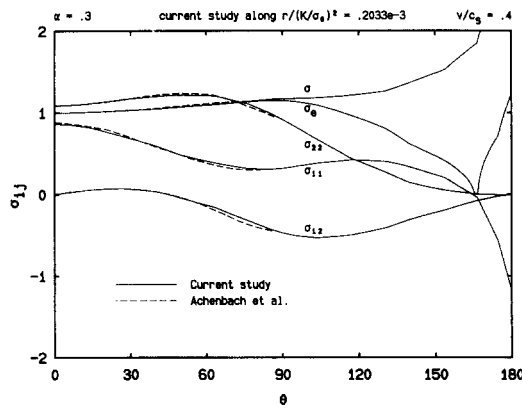
Fig. 4.3. Angular variations of the polar stress components, the effective stress σ_e, and the flow stress σ for $\alpha = 0.3$ and $v/c_s = 0.4$, normalized such that $\sigma_e = 1$ at $\theta = 0$, with comparison to the asymptotic solution by Achenbach, Kanninen and Popelar [3].

the one predicted in [3]. This estimate is reasonable since a slightly higher m value is used in [3], which, according to this study, will result in a higher unloading angle.

Using the same error tolerance, the effect of hardening and inertia on the angular extent of the crack-tip active plastic zone can be estimated from the values of σ_e and σ. For example, at $m = 0.3$, it is found that the unloading angle changes slightly from 78° for $\alpha = 0.5$ to 80° for $\alpha = 0.05$. Whereas at $m = 0.5$, it changes from 82° for $\alpha = 0.4$ to 92° for $\alpha = 0.05$. On the other hand, for the same strain hardening level $\alpha = 0.4$, the angle is estimated to be 76° at $m = 0$ and 82° at $m = 0.5$. It must be pointed out however, that the estimation is very sensitive to the choice of error tolerance, and the values given above will have different degrees of accuracy.

The effects of hardening and inertia on the angular stress variations are as follows. When crack speed is low ($m < 0.4$) or when the strain hardening level is high ($\alpha > 0.1$), the stress variations are not much different from their quasi-static counterparts (see Figs. 4.4, 4.5, and 3.4). However, when m is sufficiently high and α sufficiently low, a distinctive feature can be observed in the stress variations. For example, the stress variations are shown in Fig. 4.4 for $m = 0.5$ but different levels of strain hardening, and in Fig. 4.5 for $\alpha = 0.05$ but different crack propagation
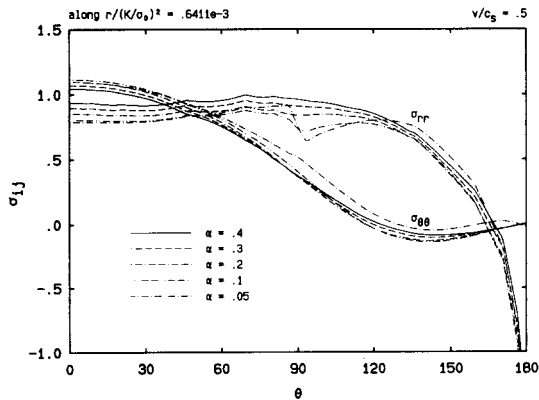
Fig. 4.4a. The effect of hardening on the angular variations of the polar stress components σ_{rr} and $\sigma_{\theta\theta}$ for $v/c_s = 0.5$, normalized such that the effective stress $\sigma_e = 1$ at $\theta = 0$.
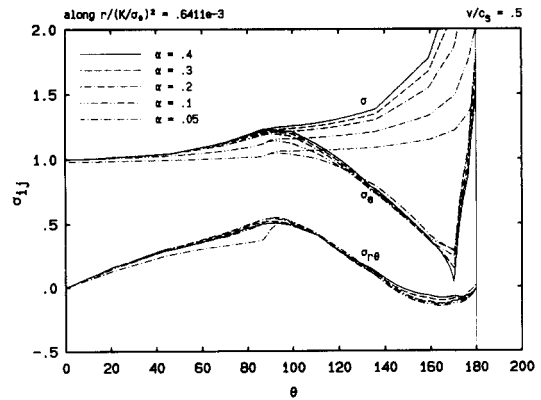
Fig. 4.4b. The effect of hardening on the angular variations of the polar stress component $\sigma_{r\theta}$, the effective stress σ_e, and the flow stress σ for $v/c_s = 0.5$, normalized such that $\sigma_e = 1$ at $\theta = 0$.
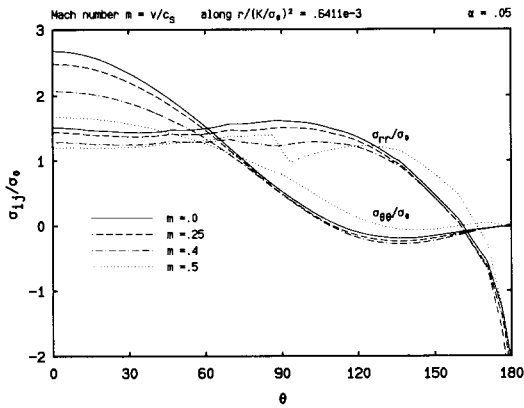
Fig. 4.5a. The effect of crack propagation speed on the angular variations of the polar stress components σ_{rr} and $\sigma_{\theta\theta}$ for $\alpha = 0.05$, in normalized form.
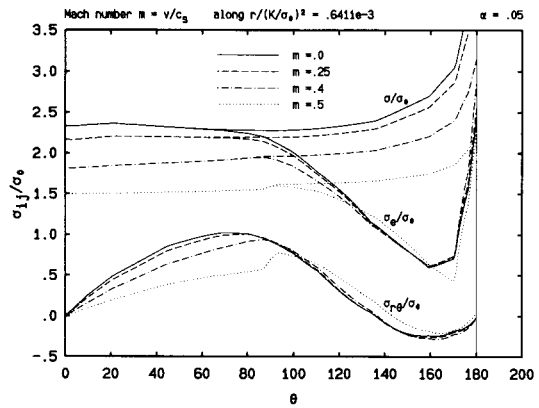
Fig. 4.5b. The effect of crack propagation speed on the angular variations of the polar stress components $\sigma_{r\theta}$, the effective stress σ_e, and the flow stress σ for $\alpha = 0.05$, in normalized form.

speeds. It is seen that when m is high and α is low, kinks or strong signs of slope discontinuity in polar stress components σ_{rr} and $\sigma_{r\theta}$ appear at locations where approximately elastic unloading is taking place. This feature also has been observed for rapid dynamic crack propagation in elastic-perfectly plastic solids (see Fig. 5(b) of [23] and the asymptotic solution of Gao [21]). This distinctive behavior, if not attributed to numerical errors, may explain an interesting situation encountered by Achenbach, Kanninen and Popelar [3]. They reported that, in carrying out the integration of a set of ordinary differential equations in their asymptotic analysis, there exist limiting crack speeds (corresponding to different values of α) above which their numerical integration algorithm fails to converge.

The existence of a secondary active plastic zone along the crack flank for $\alpha = 0.05$ is evident from Figs. 4.4b and 4.5b, where it can be seen that σ_e rises sharply near $\theta = 180°$ and eventually coincides with σ, which indicates yielding or reversed plastic loading there. For other values of α, the values of σ_e always remain lower than corresponding values of σ near the crack surface, indicating elastic states there.

Another interesting feature of angular stress variations can be observed near the prospective crack line $\theta = 0°$. It is found that as m increases, the value of $\sigma_{\theta\theta}$ decreases for all values of α considered, whereas that of σ_{rr} undergoes a transition: it increases for $\alpha \approx 0.4$ and 0, but decreases for $\alpha \approx 0.05$.

The angular variations of near-tip velocity field for various strain hardening levels and crack propagation speeds are presented in Fig. 4.6a with normalization such that $v_1 = -1$ at $\theta = 0°$, and in Fig. 4.6b with normalization as shown so that the relative magnitudes of v_1 and v_2 at different m numbers can be observed. Like stresses, velocity components have very much the same features as their quasi-static counterparts when m is small or when α is large, and are seen (from figures not shown here) to experience abrupt changes near where the active plastic zone separates the elastic unloading zone when m is sufficiently large and α sufficiently small.

4.3. Radial field variations

The effects of hardening and crack propagation speed on the radial variations of the crack-tip stress and deformation fields are presented here. To be concise, only a limited number
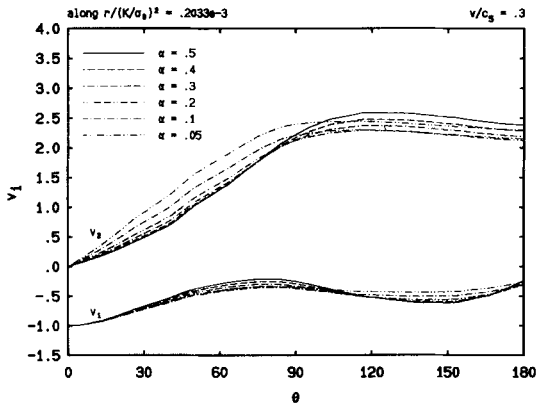
Fig. 4.6a. The effect of hardening on the angular variations of the Cartesian velocity components for $v/c_s = 0.3$, normalized such that $v_1 = -1$ at $\theta = 0$.
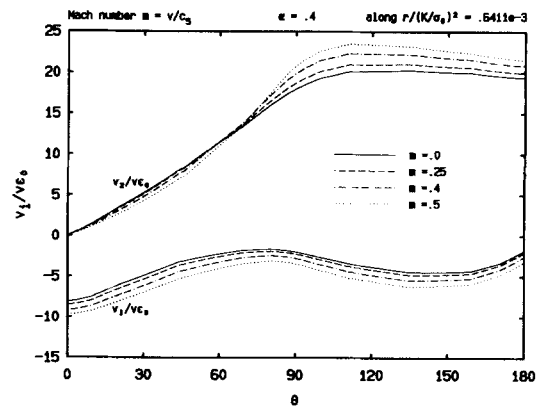
Fig. 4.6b. The effect of crack propagation speed on the angular variations of the Cartesian velocity components $\alpha = 0.4$, in normalized form.

of illustrations will be included in this paper. However, the features demonstrated are typical of variations of all similar field quantities, whose details can be found in [14].

A general observation about the radial dependence of stress and strain states is that as the crack tip is approached, stresses and strains rise rapidly, indicating stress and strain singularities at the crack tip. Like quasi-statically growing cracks, the singularities are found to be of the type r^s, r being the radial distance to the crack tip. The singularity exponent s is negative and dependent on m and α, and is given by the slope of a stress or strain vs. r curve plotted in double-logarithmic coordinates. A collection of such curves for σ_{22} are presented in Fig. 4.7a for $m = 0.3$ and various α values, and in Fig. 4.7b for $\alpha = 0.4$ and various m values. As expected, the curves are for the most part straight lines, and have negative slopes. It can be concluded that $|s|$ decreases as α decreases or as m increases. It is also noted that there are signs, although they are not obvious from the figures shown here, that as α decreases the straight stress line in the double-logarithmic coordinates starts to curve, an evidence of decreasing dominance-zone size of the r^s-type stress singularity.
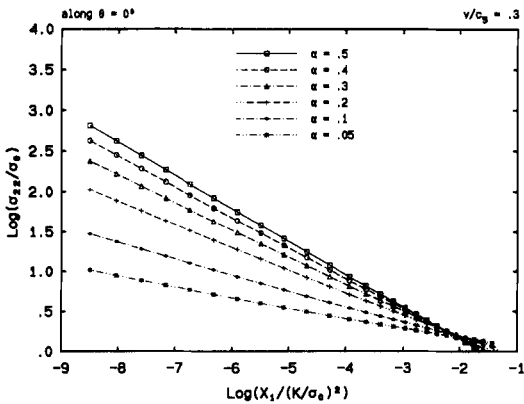
Fig. 4.7a. Radial variations of the stress component σ_{22} for $v/c_s = 0.3$ along the prospective crack line in normalized double-logarithmic coordinates.
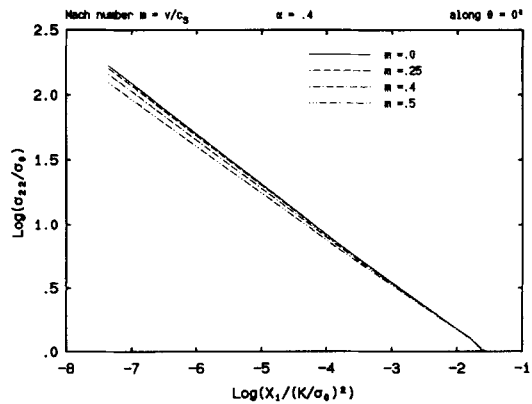
Fig. 4.7b. Radial variations of the stress component σ_{22} for $\alpha = 0.4$ along the prospective crack line in normalized double-logarithmic coordinates.

It is worth pointing out an interesting phenomenon concerning the dependence of the radial variations of σ_{11} on the level of strain hardening. While σ_{22} consistently decreases as m increases for all α values, σ_{11} reverses its tendency at a small α value. For example, for the same range of radial distance r along $\theta = 0$ where the r^s-singularity is observed, as m increases σ_{11} first increases when $\alpha = 0.4$, then decreases when $\alpha = 0.05$, and again increases when hardening disappears (see Fig. 8(b) of [23]).

To compare the values of the singularity exponent s with those of the asymptotic analysis [3], and to estimate the range of dominance of the r^s-type stress singularity, least-square fittings are performed for the finite element data extracted from the sixth to the tenth elements along the prospective crack line. As in the case of quasi-static crack growth, s is estimated for each stress component and their mean value is taken to be the final estimate. The result of the estimations are listed in Table 4.1 for $m = 0.4$ ($m \approx 0.403$ in [3]) and various α values, where s_1 is the estimate from σ_{11}; s_2 from σ_{22}; s_a is the average of s_1 and s_2; s_r is the reference value from [3]; and ε is the percentage relative difference between s_a and s_r. As is seen, the difference between finite element results and the analytic results is small.

Estimates can be made of the range of validity of the r^s-singularity in the same manner as is done for the case of quasi-static crack growth. By setting a relative error tolerance, say about 5 percent, between the original finite element data and the least-square-fitted data, the ratio of the r^s-singularity dominance zone size along $\theta = 0$ to that of the crack-tip active plastic zone is obtained and listed in Table 4.2, where R_1 and R_2 are the ratios estimated from, respectively, σ_{11} and σ_{22}, and E_1 and E_2 are the actual maximum percentage relative errors between the original and fitted data of σ_{11} and σ_{22} respectively. It is found that σ_{22} has a larger dominance zone than σ_{11}, that the range of validity of the r^s-singularity is significant for both stress components when compared with the crack-tip active plastic zone size, and that as α decreases, the dominance zone size of the r^s-singularity also decreases.

Typical radial variations of plastic strain components are presented in Fig. 4.8 for ε_{22}^p along the prospective crack line $\theta = 0$, for $m = 0.3$ and various α values. As stated before, these curves appear to be straight in the double-logarithmic coordinates. Comparing the distributions of ε_{11}^p and ε_{22}^p, it is observed (from figures not shown here) that the latter always dominates the former, although their difference becomes smaller as α or m becomes larger. It is also observed, in the normalized coordinates, that for a certain linear hardening elastic-plastic material (i.e. for a fixed α value), the magnitude of ε_{22}^p near the crack tip decreases as m increases. As a result, the level of

Table 4.1. Values of s for dynamic crack growth at $m = 0.4$

α	s_1	s_2	s_a	s_r	ε
0.5	−0.402	−0.406	−0.404	−0.411	−1.7
0.3	−0.328	−0.333	−0.331	−0.339	−2.4
0.2	−0.271	−0.276	−0.274	−0.282	−2.8

Table 4.2. Dominance-zone size for r^s-type stress singularity for dynamic crack growth at $m = 0.4$

α	R_1	E_1	R_2	E_2
0.5	0.997	4.9	1.36	4.3
0.3	0.321	4.7	1.23	4.0
0.2	0.199	4.4	0.605	4.7
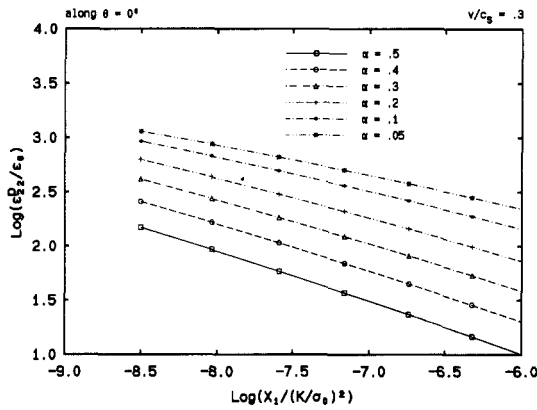
Fig. 4.8. Radial variations of the plastic strain component ε_{22}^p for $v/c_s = 0.3$ along the prospective crack line in normalized double-logarithmic coordinates.
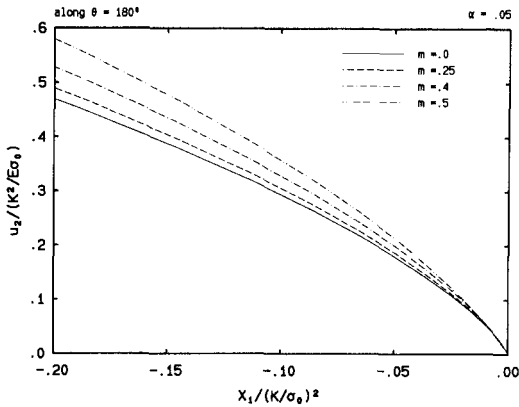
Fig. 4.9a. The effect of crack propagation speed on the radial variation of the vertical displacement u_2 along the crack surface for $\alpha = 0.05$ in normalized coordinates.
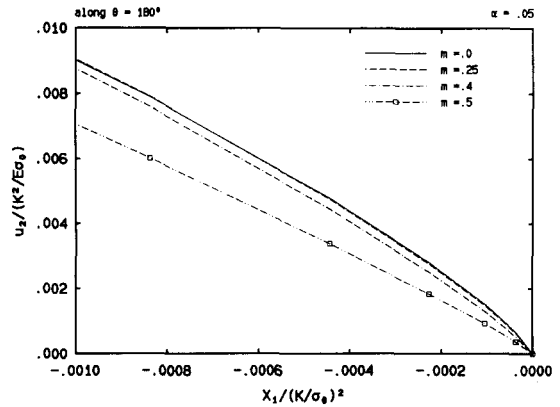
Fig. 4.9b. A detailed view of the effect of crack propagation speed on the radial variation of the vertical displacement u_2 along the crack surface for $\alpha = 0.05$ in normalized coordinates.

the effective plastic strain near the crack tip will decrease as m or crack speed increases. Thus, as demonstrated in [14, 23] for crack growth in ideally plastic solids, this asymptotic tendency of the effective plastic strain can be used to explain the following experimental observation on metallic materials: The resistance of a material to crack propagation is higher at a higher crack propagation speed. The above can be interpreted as follows. At a certain fixed load level, which is characterized by the value of the far-field stress intensity factor K, the level of plastic straining, which is represented by the effective plastic strain, is lower for higher crack propagation speeds at the same location ahead of the crack tip. Hence, in order for the level of plastic straining at a higher crack speed to reach the same magnitude as that at a lower crack speed, the loading for the former must be raised. Consequently, continued fracture will occur at a higher crack speed only if a higher loading level is achieved, if fracture is characterized by the attainment of a critical plastic strain level at a certain physical distance ahead of the crack tip (a critical plastic strain fracture criterion).

Finally we discuss the effects of strain hardening and crack propagation speed on the crack opening displacement. As in the case of quasi-static crack growth, it is found that the magnitude

of the opening displacement u_2 in the normalized coordinates decreases, for fixed m, as α decreases, and increases (at sufficient distance away from the crack tip), for fixed α, as m increases. However, for a low strain hardening material, say $\alpha = 0.05$, and at a distance very close to the crack tip, the magnitude of u_2 will decrease as m increases (compare Figs. 4.9a and 4.9b). This latter feature of the crack-tip opening displacement was more clearly observed in mode I plane strain for elastic-perfectly plastic solids in [22], at a distance to the crack tip about one-hundred times larger than that in the present study. As discussed in [14, 23], a region with this special feature and of sufficient size is necessary for one to use a critical opening displacement fracture criterion and to derive a theoretical relation between the critical K-value and the crack speed v, as is done in plane strain [22].

5. Summary

The findings of a detailed, full-field finite element investigation of quasi-static and dynamic crack growth in linear hardening elastic-plastic solids under mode I plane stress, steady state, and small-scale yielding conditions are presented. The results of the finite element study given for a variety of linear hardening materials and different crack propagation speeds, compare well with available asymptotic analyses, and reveal many features of the size and shape of the crack-tip active plastic zone and the near-tip variations of stress and deformation fields, which can be used constructively in higher-order asymptotic analysis, full-field experimental interpretations, and further numerical crack-growth simulations.

Acknowledgments

References

1. J.C. Amazigo and J.W. Hutchinson, *Journal of the Mechanics and Physics of Solids* 25 (1977) 81–97.
2. P. Ponte Castañeda, *Journal of the Mechanics and Physics of Solids* 35 (1987) 227–268.
3. J.D. Achenbach, M.F. Kanninen and C.H. Popelar, *Journal of the Mechanics and Physics of Solids* 29 (1981) 211–225.
4. V. Dunayevsky and J.D. Achenbach, *Journal of Applied Mechanics* 49 (1982) 646–647.
5. P. Ponte Castañeda, *Journal of Applied Mechanics* 54 (1987) 379–387.
6. R.H. Dean and J.W. Hutchinson, in *Fracture Mechanics: Twelfth Conference, ASTM STP 700*, American Society for Testing and Materials (1980) 383–405.
7. R.H. Dean, in *Elastic-Plastic Fracture: Second Symposium, ASTM STP 803*, American Society for Testing and Materials (1983) I-39-I-51.
8. K.K. Lo and D. Peirce, *Journal of the Mechanics and Physics of Solids* 29 (1981) 143–152.
9. J. Christoffersen and J.W. Hutchinson, *Journal of the Mechanics and Physics of Solids* 27 (1979) 465–487.
10. R. Zhang, X. Zhang and K.C. Hwang, in *Proceedings of ICF International Symposium on Fracture Mechanics* (Beijing), Science Press, Beijing, China (1983) 283–290.

11. P.S. Lam, 'Numerical analysis of stable crack growth in elastic-plastic materials in small scale and general yielding', Ph.D. thesis, University of Illinois at Urbana-Champaign (1982).

12. P.S. Lam and R.M. McMeeking, *Journal of the Mechanics and Physics of Solids* 32 (1984) 395–414.

13. J.D. Achenbach and M.F. Kanninen, in *Fracture Mechanics*, N. Perrone et al. (eds.), University Press of Virginia, Charlottesville (1978) 649–670.

14. X. Deng, 'Dynamic crack propagation in elastic-plastic solids', Ph.D. thesis, California Institute of Technology, Pasadena (1990).

15. H.L. Schreyer, R.F. Kulak and J.M. Kramer, *Journal of Pressure Vessel Technology* 101 (1979) 226–234.

16. J.R. Rice and D.M. Tracey, in *Numerical and Computer Methods in Structural Mechanics*, S.R. Fenves et al. (eds.), Academic Press (1973) 585–623.

17. D.M. Tracey, *Journal of Engineering Materials and Technology* 98 (1976) 146–151.

18. X. Deng and A.J. Rosakis, *Finite Elements in Analysis and Design* 7 (1990) 181–191.

19. J.R. Rice, in *Fatigue Crack Propagation, ASTM STP 415*, American Society for Testing and Materials (1967) 247–311.

20. J.R. Rice, in *Fracture, An Advanced Treatise*, Vol. II, H. Liebowitz (ed.), Academic Press, N.Y. and London (1968) 191–311.

21. Y.C. Gao, *International Journal of Fracture* 34 (1987) 111–129.

22. P.S. Lam and L.B. Freund, *Journal of the Mechanics and Physics of Solids* 33 (1985) 153–167.

23. X. Deng and A.J. Rosakis, *Journal of the Mechanics and Physics of Solids* 39 (1991) 683–722.